Computers and Geotechnics 128 (2020) 103848

Contents lists available at ScienceDirect

Computers and Geotechnics

journal homepage: www.elsevier.com/locate/compgeo

Research Paper

Meta-modelling of coupled thermo-hydro-mechanical behaviour of hydrate reservoir

Mingliang Zhou[a], Mahdi Shadabfar[a,*], Hongwei Huang[a], Yat Fai Leung[b], Shun Uchida[c]

[a] Department of Geotechnical Engineering, Tongji University, China
[b] Department of Civil and Environmental Engineering, The Hong Kong Polytechnic University, Hong Kong
[c] Department of Civil and Environmental Engineering, Rensselaer Polytechnic Institute, Troy, NY 12180, USA

ARTICLE INFO

Keywords:
Meta-modelling
Machine learning
Hydrate reservoir
Wellbore deformation
Thermo-hydro-mechanical model

ABSTRACT

The responses of hydrate reservoir during gas production are complex due to the spatially and temporally evolving thermo-hydro-mechanical properties. Accurate modeling of the behavior, therefore, requires a coupled multiphysics simulator with a large number of parameters, leading to substantial computational demands. This makes it challenging to efficiently predict long-term reservoir responses. In this study, by utilizing an artificial neural network (ANN) algorithm, a meta-model is proposed to deep learn the relationship between the material properties and reservoir responses, including borehole displacement and fluid production. As such, a set of 950 coupled thermo-hydro-mechanical simulations of a one-layer sediment axisymmetric model is carried out for six-day gas production via depressurization. Eighteen input parameters are considered in each simulation covering four physical aspects, namely hydrate dissociation, thermal flow, fluid flow, and mechanical response. With this comprehensive dataset of the responses, a meta-model is established based on the trained neural network, resulting in an efficient prediction of the responses with significantly reduced computational demand. The model is then further utilized to predict the future reservoir responses, and it is found that the results are in a good agreement with those from the fully-coupled simulator.

1. Introduction

Methane hydrate is a clatherate compound consisting of methane gas and water molecules, which exists under high pressure and low temperature conditions, such as deep sea or permafrost regions. When such pressure–temperature condition is varied and moves outside the stability zone, phase change occurs where the solid hydrate dissociates into methane gas and water, thereby enabling extraction of methane gas as a potential energy source. More than 200 gas hydrate sites have been identified around the world (Makogon and Omelchenko, 2013; Kvenvolden and Rogers, 2005), and many consider them as a possible option to meet the growing energy demands (Kvenvolden, 1988; Kvenvolden, 1998; Boswell, 2009; McCartney et al., 2016). There have been a number of field-scale gas production tests from gas hydrate-bearing sediments, including those in Canada (Hancock et al., 2005; Dallimore et al., 2012), USA (Anderson et al., 2011; Schoderbek et al., 2013), China (Wang et al., 2014) and Japan (Yamamoto et al., 2014). Therefore, characterization of hydrate reservoirs and investigation of their behaviors under various field conditions and operational procedures have attracted substantial research interests.

Gas production from hydrate reservoir involves dissociation of hydrates and the ensuing fluid flows towards the production well. This accompanies the consolidation process that leads to deformations of the sediments and also changes in the permeability. The multiphysics processes entail unsaturated soil mechanics and seepage phenomena, triggered by pressure- or temperature-induced hydrate dissociation which is an endothermic reaction. Meanwhile, the dissociation of hydrate also affects the structure of the hydrate-bearing sediments and leads to changes in their strength and stiffness (e.g. Uchida et al., 2012; Uchida et al., 2016). Simulations of such coupled thermo-hydro-mechanical processes have been reported by various researchers (Sun et al., 2005; Liu and Flemings, 2007; Kimoto et al., 2007; Rutqvist et al., 2009; Moridis et al., 2011; Kim et al., 2012; Klar et al., 2013; Gupta et al., 2015; Uchida et al., 2016; Sánchez and Santamarina, 2017; Shen et al., 2016; Jiang et al., 2016; Sánchez et al., 2017). Among the various approaches and constitutive models, simulating this complex coupled processes is often computationally demanding and requires a large number of material parameters to represent multiple facets of the

* Corresponding author.
E-mail addresses: zhoum@tongji.edu.cn (M. Zhou), mahdishadabfar@tongji.edu.cn (M. Shadabfar), huanghw@tongji.edu.cn (H. Huang), andy.yf.leung@polyu.edu.hk (Y.F. Leung), uchids@rpi.edu (S. Uchida).

https://doi.org/10.1016/j.compgeo.2020.103848
Received 16 December 2019; Received in revised form 23 August 2020; Accepted 17 September 2020
Available online 06 October 2020

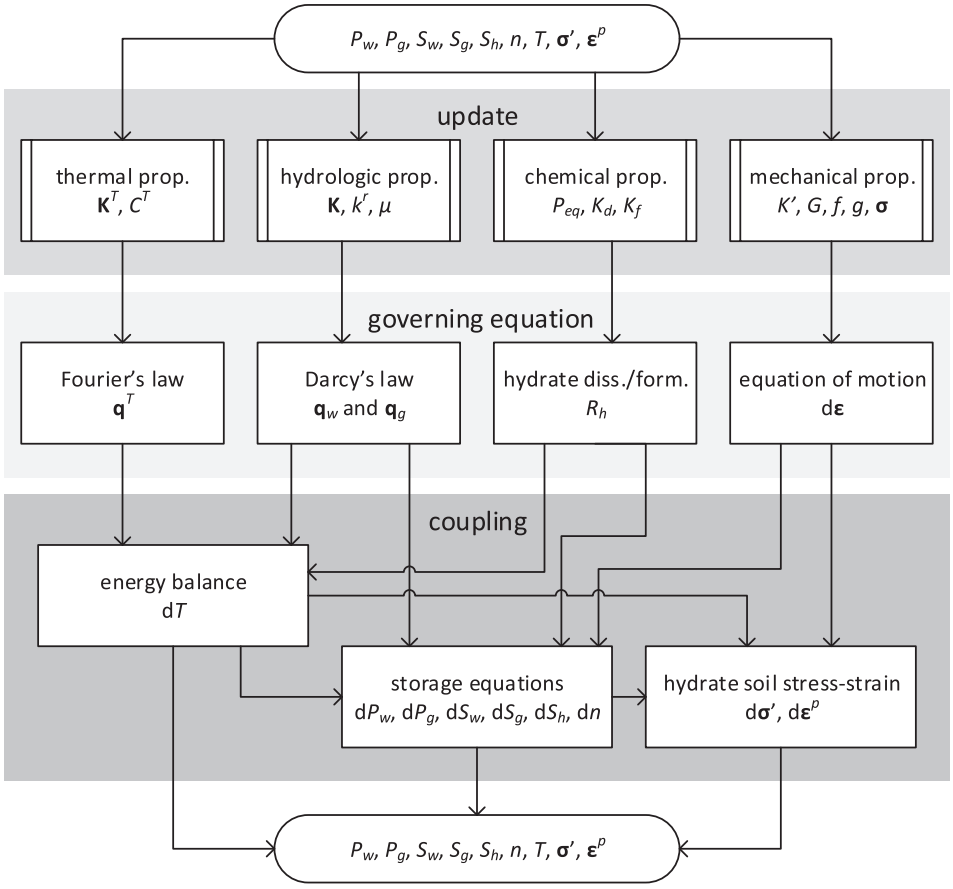

Fig. 1. Single calculation cycle by the adopted *FLAC* THM simulator.

hydrate reservoir behavior. In addition, heterogeneity and uncertainties of in situ material properties affect the accuracy of model predictions to various extents (Zhou et al., 2018). These uncertainties are compounded by the temporal changes in the sediment properties as hydrate dissociates, both hydrologic and mechanical properties of the sediments are altered to different degrees (Waite et al., 2009; Zhou et al., 2018). Therefore, accurate predictions of hydrate reservoir responses are difficult, while probabilistic approaches normally involve large numbers of analyses, and are hampered by significant computational demands associated with the coupled thermo-hydro-mechanical simulations.

Recent years have seen substantial developments in the field of machine learning, particularly the development of neural network models, for predictions of complex system behaviors including those in various engineering disciplines. Some examples in civil engineering include predictions of structural element behavior and building response (Bal and Buyle-Bodin, 2013; Kewalramani and Gupta, 2006; Li et al., 2011), groundwater level forecasting (Adamowski and Chan, 2011) and cost estimates of infrastructure projects (Cheng et al., 2010; Hola and Schabowicz, 2010). Applications of machine learning methods in geotechnical engineering range from predictions of soil and rock properties (Goh, 1995; Yilmaz and Kaynar, 2011; Asghari et al., in preparation), to approximations of system response for foundations (Goh, 1996; Abu Kiefa, 1998; Shahin et al., 2002; Momeni et al., 2015; Pooya Nejad and Jaksa, 2017), slopes and retaining structures (Goh et al., 1995; Ni et al., 1996; Tien Bui et al., 2016). Many of these previous studies took advantage of machine learning algorithms to reveal patterns of soil variability or field measurements of system response. However, such approach may not be feasible for the investigation of hydrate reservoir behaviors during gas production operations, since there are only a handful of field tests around the world so far and the number of data points is very limited. To date, only a few attempts of machine learning applications have been reported on hydrate reservoir characterizations. These applications include prediction of the distribution of hydrocarbon reservoirs (Lee et al., 2017; Lin et al., 2018), classification of the reservoir facies (Saikia et al., 2019), and prediction of reservoir lithology (Singh et al., 2019). There has been no published work in the literature on the use of machine learning in predicting the hydrate reservoir behaviour related to the production response.

Considering these unique features and challenges of gas hydrate studies, this paper proposes a meta-modelling approach using neural network, which is trained by a synthetic dataset produced by a series of coupled numerical simulations. In the subsequent sections, the multi-physics aspects of gas production from hydrate bearing sediments will be described, through governing equations of the thermo-hydro-mechanical simulations and the associated material parameters. The training and testing data for the neural networks are produced by a series of coupled thermo-hydro-mechanical simulations, where the material parameters are varied across the multi-dimensional sample space. The neural network approach for meta-modelling will then be introduced, and illustrated with a hypothetical scenario of gas production from a hydrate reservoir. The meta-model represents the relationships between material properties (i.e., thermo, hydrologic and geomechanical properties of hydrate-bearing sediments) and the reservoir response (i.e., gas and water production and borehole displacements), and is capable of reproducing the results from coupled simulations with much higher computational efficiency. The robustness of the meta-model is also demonstrated through predictions of the reservoir response beyond the time frame of the synthetic training data.

2. Thermo-hydro-mechanical simulation of hydrate reservoir

2.1. Overview of the FLAC thermo-hydro-mechanical simulator

To create the synthetic dataset to train the neural network, this study utilizes the thermo-hydro-mechanical formulation originally developed by (Klar et al., 2013) for hydrate-bearing sediments. This formulation was implemented by (Klar et al., 2013) into a commercial finite difference program, *FLAC* (Itasca Consulting Group), using the programming language *FISH* that is embedded within *FLAC* to enable definition of new variables and functions associated with hydrates. Herein, this numerical tool is referred to as the *FLAC* THM (thermo-hydro-mechanical) simulator in this study. Apart from the built-in equation of motion, the *FLAC* THM simulator solves the newly-defined governing equations as well as the coupled equations. Fig. 1 presents how the *FLAC* THM simulator solves these governing equations in a single calculation cycle. Each calculation cycle begins with known state variables including pressures, saturations, porosity, temperature, effective stress, and plastic strain. Based on these state variables, thermo-hydro-chemo-mechanical parameters are updated such as (from left to right) bulk thermal conductivity, intrinsic permeability, hydrate phase equilibrium pressure and the stiffness of hydrate-bearing soil. Next, *FLAC* THM simulator solves the governing equations independently for each thermo-hydro-chemo-mechanical component to determine heat flux, fluid fluxes, hydrate dissociation/formation rate and incremental strain. Finally, these quantities are then used to solve coupled equations, deriving increments of the state variables. Detailed description of each equation can be found in (Klar et al., 2013).

The simulator used in this study is an extended version of the work by (Klar et al., 2013). It includes the effect of residual saturations on the multiphase flow and adopts the hydrate-bearing soil model that captures volumetric yielding. It has been used to analyze the responses of actual gas hydrate reservoirs during field-scale gas production tests, for example, at the Mallik gas hydrate site in 2007 and 2008 (Uchida et al., 2012) and also at the Eastern Nankai Trough in 2013 (Zhou et al., 2018). The simulator has been shown to be capable of matching fluid production history and also of revealing the effects of mechanical response on the reservoir behavior. In this coupled formulation, the effective water saturation, S_e, is given by:

$$S_e = \frac{S_w - S_{rw}(1 - S_h)}{(1 - S_{rw} - S_{rg})(1 - S_h)} \tag{1}$$

where S_{rw} and S_{rg} are the residual water and residual gas saturation, respectively, and S_h and S_w are hydrate and water saturation, respectively. This leads to the modification of relative permeability relations by (van Genuchten, 1980), so that the volumetric fluxes for the multiphase flow are given by:

$$\mathbf{q}_w = -k_w^r \frac{\mathbf{K}(1 - S_h)^N}{\mu_w}(\nabla P_w - \rho_w \mathbf{g}) \tag{2}$$

$$\mathbf{q}_g = -k_g^r \frac{\mathbf{K}(1 - S_h)^N}{\mu_g}(\nabla P_g - \rho_g \mathbf{g}) \tag{3}$$

$$k_w^r = S_e^b [1 - (1 - S_e^{1/a})^a]^2 \tag{4}$$

$$k_g^r = (1 - S_e)^c (1 - S_e^{1/a})^{2a} \tag{5}$$

where $\mathbf{q}$ is the volumetric flux, k^r is the relative permeability factor, $\mathbf{K}$ is the intrinsic permeability, N is the power to correlate the intrinsic permeability with effective permeability (Masuda et al., 1999), μ is the viscosity, P is the pressure, ρ is the density, with the subscript g and w representing gas and water, respectively. $\mathbf{g}$ is the gravitational vector, and a, b and c are the van Genuchten model parameters for the relative permeability factor (van Genuchten, 1980). Through the effective water saturation, the residual saturations also affect the development of capillary pressure, P_c:

$$P_c = P_g - P_w = P_0 (S_e^{-1/a} - 1)^{1-a} \tag{6}$$

where P_0 is the air entry pressure.

Mechanical behavior is modeled by the methane hydrate critical state model (Uchida et al., 2012; Uchida et al., 2016). As the model adopts an associated flow rule, the yield function, f, and the plastic potential, g, are identical and given by:

$$f = g = q^2 + M^2 p' [p' - R(p'_{cs} + p'_{cd})] \tag{7}$$

where q is the deviator stress, p' is the mean effective stress, M is the stress ratio ($= q/p'$) at the critical state, R is the subloading ratio to accommodate smooth transition from elastic to plastic state (Hashiguchi, 1989), p'_{cs} is the preconsolidation stress of the host soil, p'_{cd} is the increase in the preconsolidation stress due to presence of hydrate. The evolution of R, p'_{cs} and p'_{cd} are given by:

$$\mathrm{d}R = -u \ln(R) |\mathrm{d}\, \epsilon^p| \tag{8}$$

$$p'_{cs} = \exp\left(\frac{1}{(\lambda - \kappa)(1 - n)} \epsilon_v^p\right) p'_{cs0} \tag{9}$$

$$p'_{cd} = \alpha [\exp(-m\, \epsilon_d^p) S_h]^\beta \tag{10}$$

where u is the property that determines the evolution of subloading ratio, ϵ^p is the plastic strain vector, n is the porosity, λ is the slope of compression line, κ is the slope of reloading line, ϵ_v^p is the plastic volumetric strain (compression positive), p'_{cs0} is the initial preconsolidation stress of the host soil, ϵ_d^p is the plastic deviatoric strain, m is the parameter incorporates degradation of mechanical contribution of solid hydrate caused by deviatoric deformation, and α and β determines the increase in the preconsolidation stress due to hydrate. The contribution of hydrate to elastic modulus is given by:

$$K' = \frac{p'}{(1 - n)\kappa} + \frac{E_{h0}}{3(1 - 2\nu)} \exp(-m\, \epsilon_d^p) S_h \tag{11}$$

where K' is the bulk modulus of hydrate-bearing soil, E_{h0} is the increase in Young's modulus due to presence of hydrate and ν is the Poisson's ratio of hydrate-bearing soil.

In order to create the synthetic dataset, this study varies 18 parameters that constitute the aforementioned hydro-mechanical properties described in Eqs. (1)–(11)), and these are listed in Table 1. In total, there are approximately 40 more thermo-hydro-chemo-mechanical properties required to conduct the coupled analyses by *FLAC*, and they are summarized in Table A.1. While all material properties may entail certain degrees of variation, it is assumed in this study that the 40 other physical or chemical properties are associated with less uncertainty. Admittedly, the precise values of those parameters may also affect the reservoir behaviour. These effects are, however, not considered within the scope of this study, which focuses on the geo-mechanical and hydrological behavior and their coupled effects.

2.2. Model geometry and reservoir response

Fig. 2 presents the model geometry of a homogeneous hydrate reservoir, adopted herein for creation of the synthetic dataset. From the modeling perspective, a reservoir with thick production zone can be simplified into a single radial layer without thermal or fluid flow in the vertical direction. The depth of the considered layer is assumed to be at 1300 m below sea level and 300 m below sea floor, corresponding to the initial pore water pressure of 13 MPa and the initial effective vertical stress of 3 MPa. The initial effective horizontal stress is assumed to be 1.5 MPa. The initial porosity is 0.35, the initial temperature is 285 K and the initial hydrate saturation is 50 %. These conditions are similar

Table 1
18 model parameters selected for this study.

name	symbol	eq.	mean	max	min
		Hydrologic (8)			
initial intrinsic permeability	$\|\|\mathbf{K}\|\|$	(2), (3)	10^{-13} m^2	$10^{-11.8}$ m^2	$10^{-14.2}$ m^2
effective permeability power	N	(2), (3)	6.0	7.2	4.8
air entry pressure	P_0	(6)	10 kPa	12 kPa	8 kPa
van Genchten parameter	a	(4), (5), (6)	0.70	0.84	0.56
van Genchten parameter	b	(4)	0.5	0.6	0.4
van Genchten parameter	c	(5)	0.5	0.6	0.4
residual water saturation	S_{rw}	(1)	0.30	0.36	0.24
residual gas saturation	S_{rg}	(1)	0.25	0.30	0.20
		Mechanical (10)			
critical state stress ratio	M	(7)	1.30	1.56	1.04
slope of swelling line	κ	(9), (11)	0.010	0.012	0.008
Poisson's ratio	ν	(11)	0.30	0.36	0.24
slope of compression line	λ	(9)	0.15	0.18	0.12
initial preconsolidation stress	p'_{cs0}	(9)	6.0 MPa	7.2 MPa	4.8 MPa
hydrate dependent strength	α	(10)	20 MPa	24 MPa	16 MPa
hydrate dependent strength	β	(10)	1.0	1.2	0.8
subloading ratio evolution	u	(8)	exp(4.0)	exp(4.8)	exp(3.2)
hydrate dependent modulus	E_{h0}	(11)	10 GPa	12 GPa	8 GPa
hydrate degradation factor	m	(10), (11)	10	12	8

to those observed from the actual hydrate reservoirs (Uchida et al., 2012; Uchida et al., 2016). Under the initial temperature, the phase equilibrium pressure $P_{eq0} \approx$ 9.8 MPa and therefore there is no gas under the initial condition (i.e., $S_{g0} = 0$ and $P_{w0} = P_{g0}$). The well is assumed to be open-hole completion with an initial radius of 0.15 m, which allows deformation of the borehole. This is represented by the total stress boundary at the well which is equal to the well pressure. The well pressure, P_{well}, decreases linearly from the initial total radial stress of 14.5 MPa to 5 MPa, at the rate of 4 MPa/day to simulate the depressurization process that follows the well-boring. The pore fluid starts to flow into the well once the well pressure becomes lower than the initial pore water pressure (= 13 MPa), occurring at 0.375 day. The outer model boundary is set at 50 m, where the pore pressure, the total radial stress and temperature remain unchanged. The layer is radially discretized into 20 elements with the size of 0.15 m adjacent to the well, and increasing at a ratio of approximately 1.24.

Table 1 also shows the mean values of the 18 parameters, which are based on values reported in previous studies on actual hydrate reservoirs (Uchida et al., 2012; Uchida et al., 2016). The maximum and minimum values of the ranges are taken as ±20% of the mean values. It is important to state that the parameter values, and the associated ranges in Table 1, may be considered as 'site specific' parameters, in a way similar to the model geometry and other site conditions. Subsequently, the established meta-model is applicable only to these site conditions and parameter ranges. By demonstrating the capabilities of meta-modelling approach through this study, it becomes possible to work towards developing universal model for various site conditions in a future study.

It should also be noted that among the 58 properties used to define the analyses (Table 1 and Table A.1), some are model parameters of the constitutive relationship (e.g., specific heat, bulk modulus, and critical state stress ratio) while others are state variables that represent specific site conditions (e.g., initial stress conditions, porosity, hydrate saturation, temperature). While the state variables are important factors that affect the reservoir responses during production, their initial values are treated as known quantities for a target location at a specific site, and are therefore not considered as varied inputs in the meta-model development in this study. These state variables during gas production are constantly updated within the *FLAC* THM simulator.

Fig. 3 presents spatial and temporal changes in the thermo-hydro-mechanical state variables over a six-day period of gas production, when the mean values are adopted. At $t = 1$ day, the well pressure is 10.5 MPa, which is above the initial phase equilibrium pressure (Fig. 3a). Thus, no hydrate dissociation occurs and S_h remains at 50%, so does S_w while S_g remains at zero (Fig. 3b). During well-boring process from $t = 0$ to 0.375 days, the borehole contracts due to the decrease in the well pressure, leading to the increase in q under constant p' as the effective radial stress reduces while the effective circumferential stress increases by the same amount. After $t = 0.375$ days when the well pressure becomes lower than the in situ pore pressure, p' starts to increase while q keeps increasing, especially at the well boundary. This results in the increase in q/p' at the well boundary from its initial value of 0.75 (Fig. 3c). On the other hand, the sediments away from the well experience an increase in p' due to depressurization while developing relatively small q due to relatively small radial displacement, leading to the decrease in q/p' (Fig. 3c). At $t = 2$ days, the well pressure is 6.5 MPa and hydrate dissociation occurs. When hydrate is present, the pore gas pressure can only reach as low as the phase equilibrium pressure. Therefore, P_w (= $P_g - P_c$) and P_{eq} are almost identical in the area where hydrate dissociation is ongoing, up to $r \approx 2$ m (Fig. 3a). Due

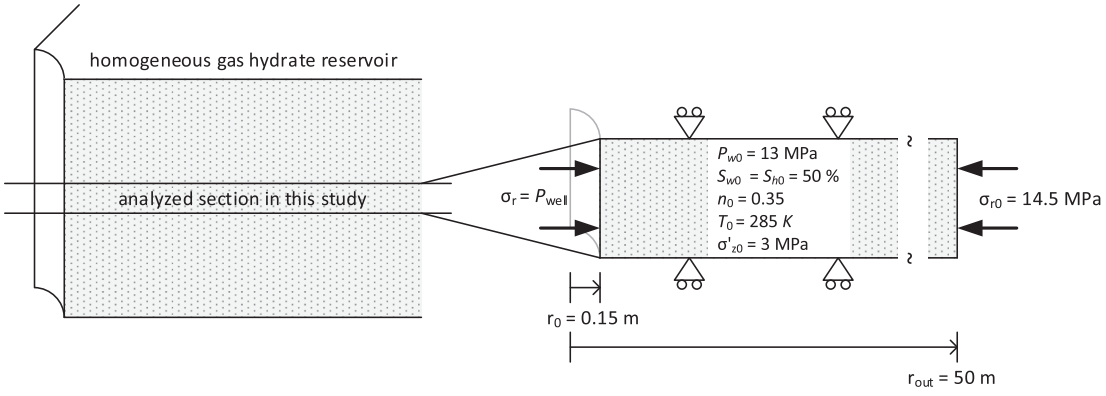

Fig. 2. Hydrate reservoir considered for this study.

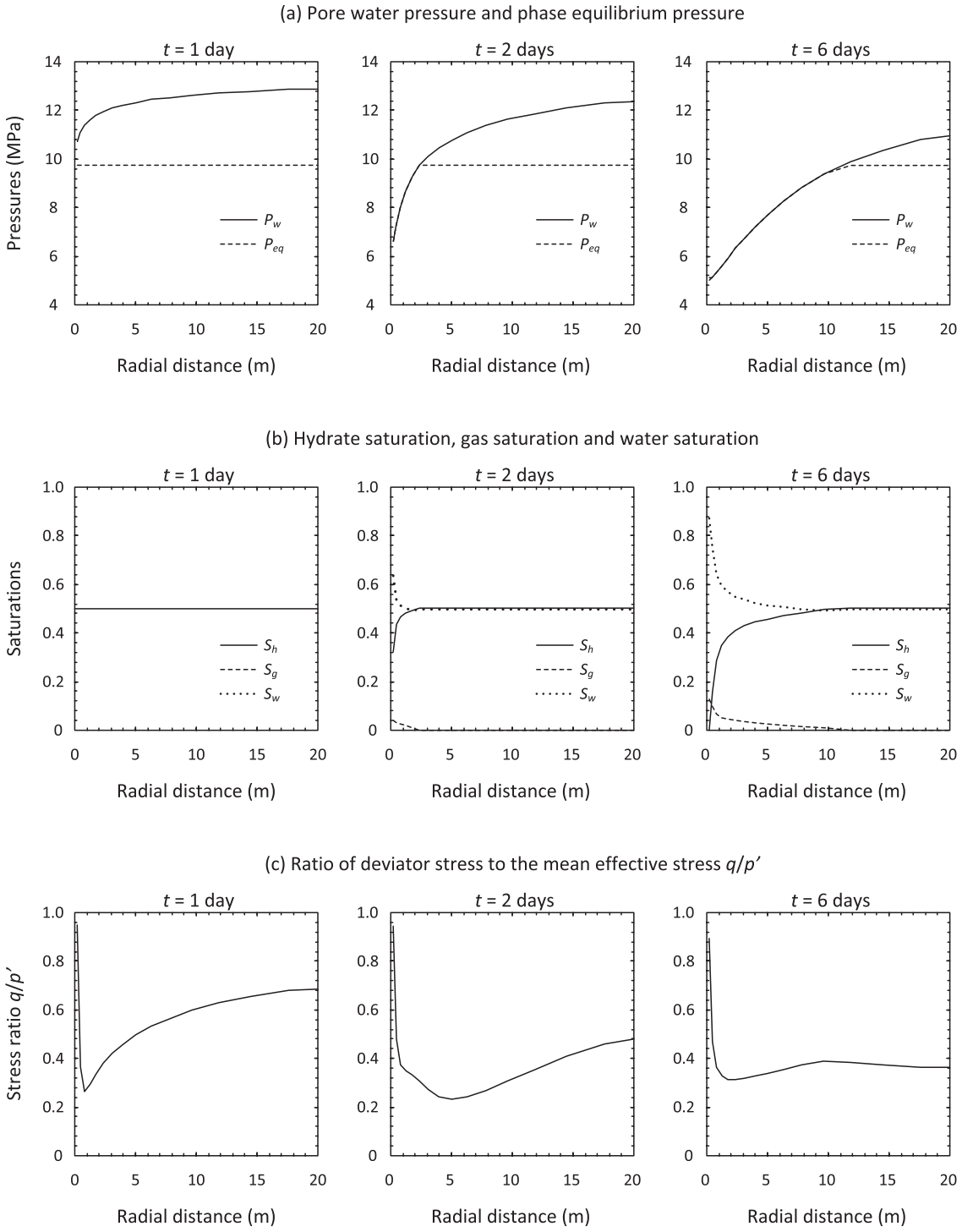

Fig. 3. Spatial and temporal changes in (a) hydrate, gas and water saturation; (b) pore water pressure and the phase equilibrium pressure; and (c) stress ratio.

to the endothermic nature of hydrate dissociation, the phase equilibrium pressure decreases, where hydrate dissociation occurs. Both P_w and P_{eq} are the lowest near the well simply because the temperature is lowest, as it is associated with the largest amount of hydrate dissociation, i.e., the smallest S_h (Fig. 3b). The value of q/p' reduces further away from the well due to depressurization that leads to increase in p' (Fig. 3c). This implies that the sediments away from the well deform more in a volumetric manner. At $t = 6$ days, the well pressure is 5 MPa, inducing more reduction of P_w as well as P_{eq} (Fig. 3a). Correspondingly, more hydrate dissociation is evident (Fig. 3b), accompanied by larger volumetric deformation (Fig. 3c).

Fig. 4 presents the reservoir responses in terms of histories of produced gas (in mass per unit height per unit radian), produced water (in mass per unit height per uni radian), and borehole displacement for 6 days, evaluated at 0.2-day time intervals. Unlike conventional gas reservoir, hydrate reservoir does not contain gas at the initial state. In

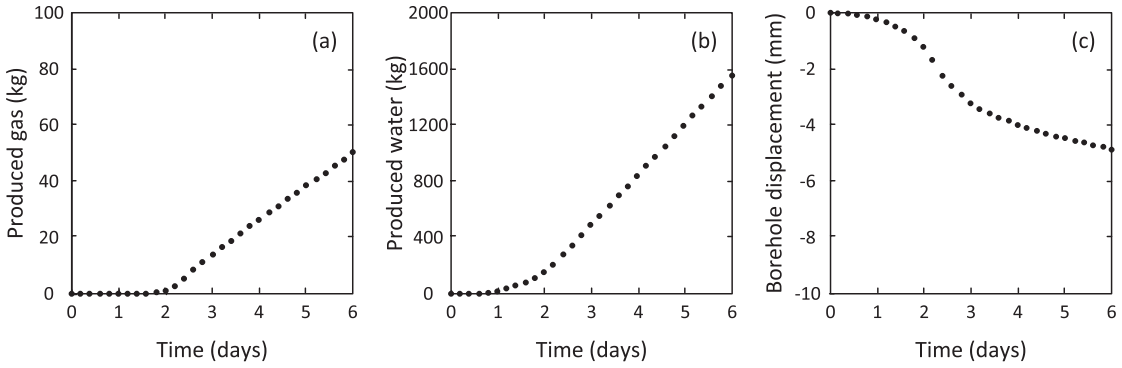

Fig. 4. Response in terms of (a) gas production, (b) water production and (c) borehole displacement.

this study, hydrate dissociation commences at around $t = 2$ day so that gas production becomes visible only after $t = 2$ days (Fig. 4a). According to Eqs. (2),(3), the permeability of the sediments reduces with the presence of hydrate, which also means the sediments become more permeable with hydrate dissociation, leading to the increase in the rate of water production (Fig. 4b). As the stiffness and strength of the sediments are also hydrate-dependent, the rate of borehole displacement also increases when hydrate dissociation commences, as shown in Fig. 3c. Although the displacement rate reduces after $t \approx 3$ days, the borehole displacement keeps developing. This implies that the stress state of the reservoir continues to evolve even after the well pressure becomes constant, due to the ongoing hydrate dissociation away from the well that reduces the sediment stiffness and strength, increases the sediment permeability and hence reduces pore pressure.

2.3. Synthetic data creation

To development the meta-model, this study creates synthetic data numerically through varying 18 material properties (Table 1) and obtaining the corresponding reservoir responses, namely, the amount of produced gas, produced water and borehole displacement, an example of which is presented in Fig. 4.

There are a number of approaches to sample a multi-dimensional parameter space, such as Latin hypercube sampling, and generations of Halton sequence or Sobol' sequence (McKay et al., 1979; Halton, 1960; Sobol', 1967). This study utilizes the sampling method adopted by (Morris, 1991) because of its capability of comprehensive sampling with relatively small number of simulations. In this method, the k parameters (i.e. the 18 varied parameters in Table 1) associated with an output Y (i.e., gas and water production and borehole displacements) are normalized and mapped to a k-dimensional unit cube. The cube is then discretized into p levels, leading to p^k crosspoints. Out of these crosspoints, $p - 1$ sampling points are selected to form a trajectory. Between two adjacent sampling points on one trajectory, only one dimension is varied by a predetermined step Δ. The direction of the step can be randomly selected. In this study, the number of investigated parameters is $k = 18$, while $p = 20$ and 50 trajectories are adopted to thoroughly search the sampling space. $\Delta = 0.5p/(p - 1)$ based on the recommendations by (Morris, 1991), and these settings lead to altogether 19 sampling points multiplied by 50 trajectories, resulting in 950 cases.

It is worth noting that this sampling approach does not explicitly consider the potential correlation among the parameters, such as the positive correlation between λ and κ. It may be possible to include such cross-correlation effects, by modifying the current method or adopting alternative methods that incorporate multivariate distribution. However, both approaches would lead to additional sampling parameters to be defined or assumed, i.e., the cross-correlation coefficients between the 18 parameters. Many of these coefficients have not been widely studied and would likely introduce more uncertainty into the analyses, and the drawbacks may outweigh the advantages of the current approach, which covers the sampling space comprehensively through the multiple sampling trajectories. Arguably, some uncommon (but not necessary impossible) combinations of parameters may arise in this process, e.g., a high λ value together with a low κ value. In fact, even if cross-correlation coefficients are introduced into the framework, such combinations can still arise when generating correlated random variables. In this study, such combinations are not ruled out simply based on intuition or experience, as long as the ranges of parameters (upper and lower bounds) are physically feasible. Perhaps more importantly, the key objective of the sampling approach is to cover the entire sampling domain, and the focus of this work is to show that ANN is capable of constructing an accurate meta-model for various combinations. The outcome of this process and the accuracy of ANN would not be affected by assumptions of cross-correlation between parameters.

Subsequently, with the *FLAC* THM simulations described earlier, these 950 cases provide history of reservoir responses, including gas production, water production and borehole displacement, recorded at every 0.2 days for a 6-day period. As a result, at every recorded time there are 17100 data points regarding material properties (950×18), which are "inputs" for the neural network, and also 2850 data points regarding reservoir responses (950×3), which are "targets" for the neural network. This dataset is visualized in Fig. 5.

3. Neural network approach to construct meta-model

The objective of the meta-model is to predict the reservoir responses for a desired period of time from any arbitrary combination of the eighteen input model parameters. To this end, two blocks of artificial neural networks (ANNs) are utilised in this study, hereinafter referred to as the first- and the second-block ANN, respectively. A schematic diagram of the meta-model is shown in Fig. 6. The first-block ANN of the meta-model predicts the reservoir responses at each recorded time, which is the time point (i.e., 0.2-day, 0.4-day, …, 6-day) when the corresponding FLAC simulation outputs are recorded. The second-block ANN of the meta-model uses the six-day continuous data points obtained from the first-block ANN to establish a time series predictor that anticipates the future reservoir responses beyond the six days.

3.1. The ANN for THM responses

The first-block ANN is developed to approximate the gas production, the water production, and the borehole displacement at any

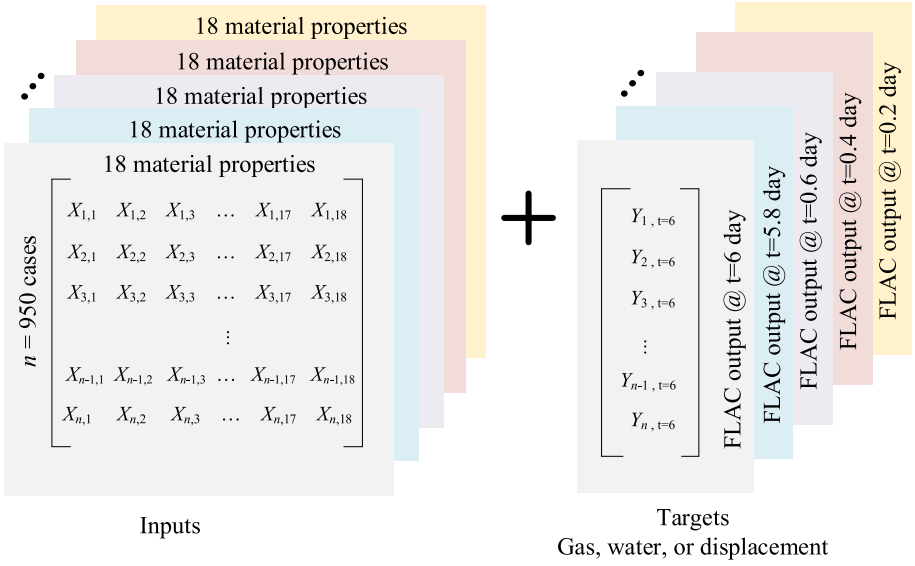

Fig. 5. Dataset constructed for training and testing the neural network.

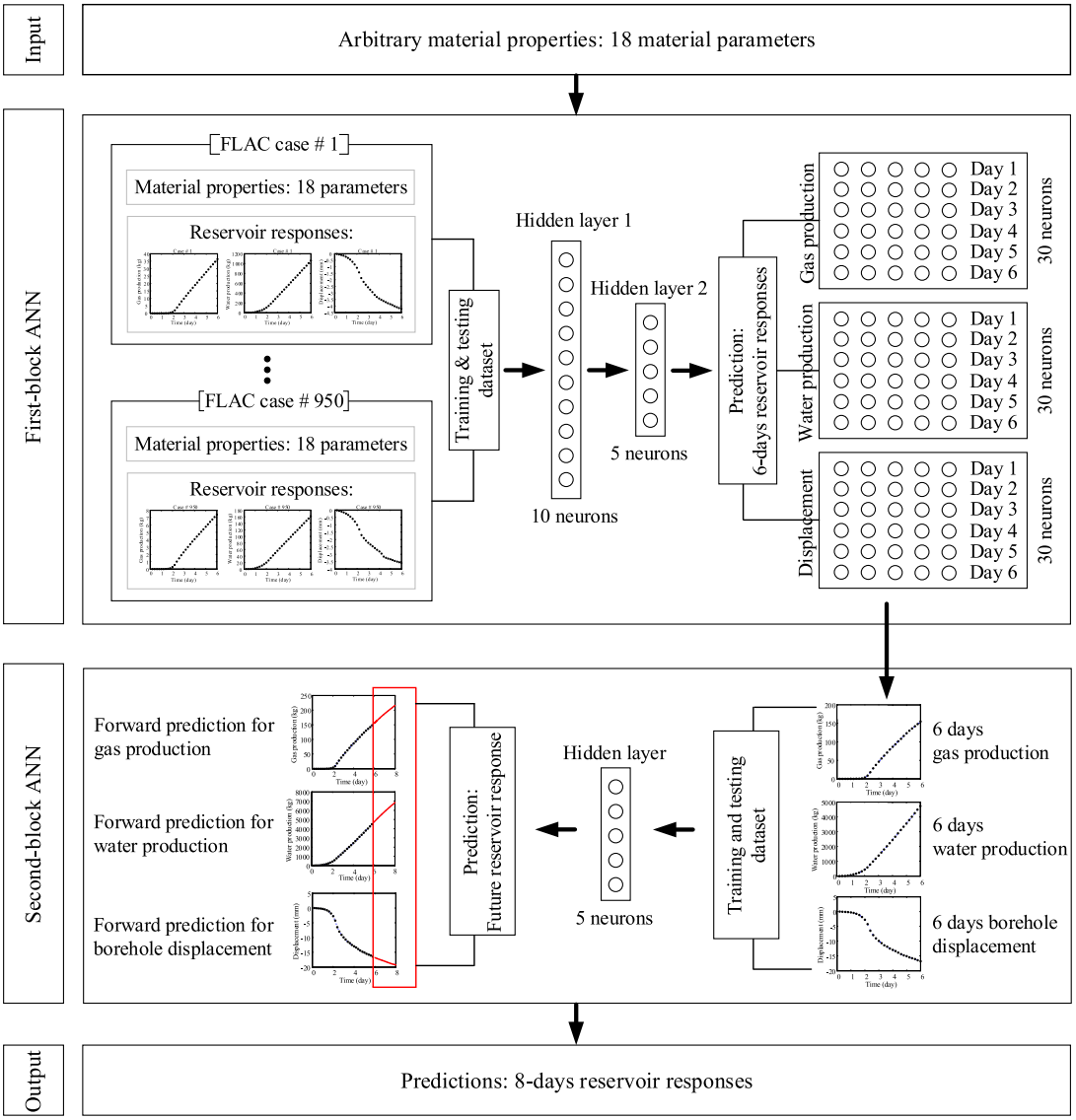

Fig. 6. The schematic diagram of the meta-model.

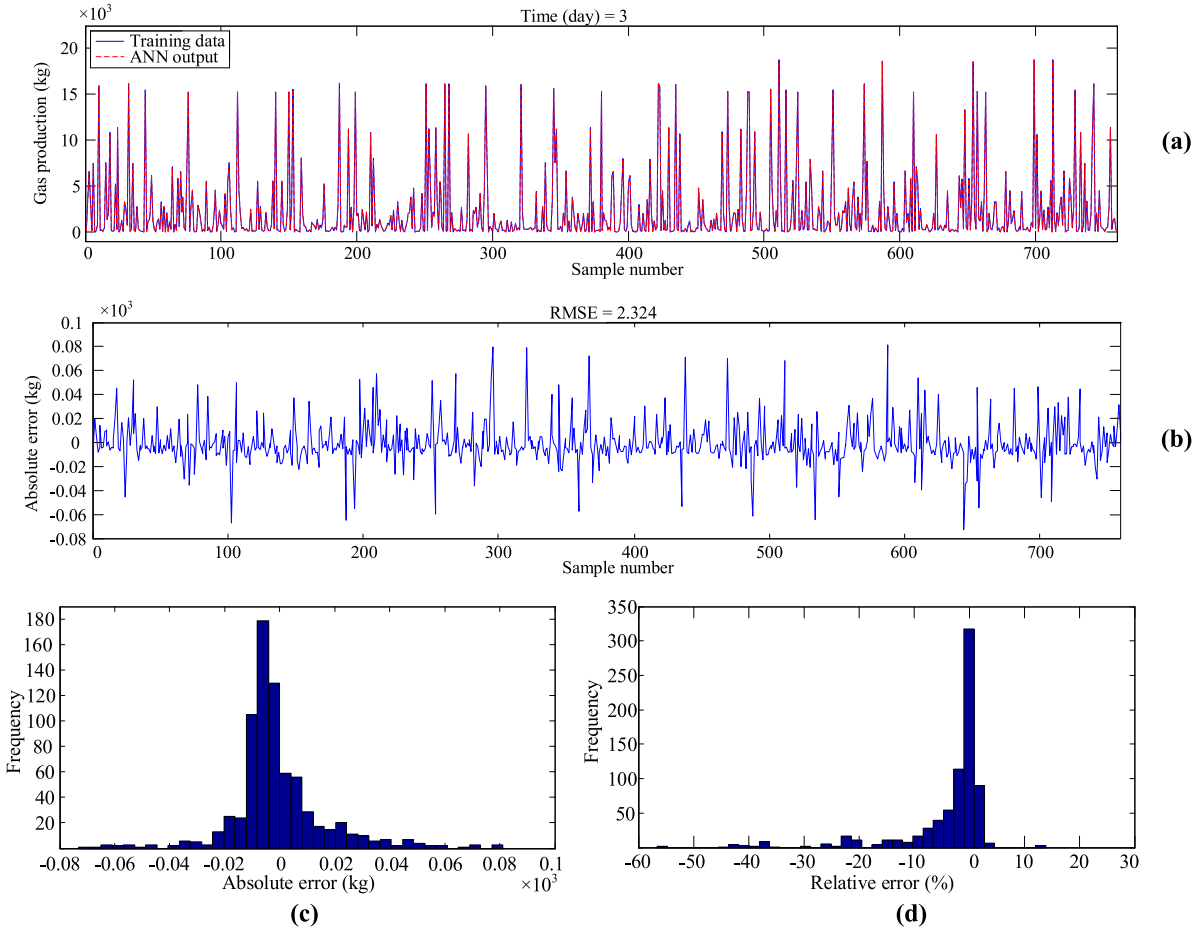

Fig. 7. The analysis output for training data, reporting (a) primary training data versus ANN results for t = 3 days, (b) the absolute error, (c) the absolute error histogram, and (d) the relative error histogram.

recorded time within the first 6 days. It is implemented in four steps: (1) Data pre-processing, (2) Establishment of the overall network structure, (3) Network training, and (4) Assessment of the first-block ANN accuracy.

The first step is to pre-process the data, including 18 different material properties for 950 cases and their corresponding *FLAC* outputs, namely gas production, water production, and borehole displacement over six days. Before using the dataset, the material properties and the reservoir responses at every 0.2 days are stored in different vectors, and the maximum and minimum values of each variable are calculated. Then, the dataset is normalized as follows:

$$X^*(i) = 2\left(\frac{X(i) - X_{min}(i)}{X_{max}(i) - X_{min}(i)}\right) - 1 \tag{12}$$

$$Y^*(i) = 2\left(\frac{Y(i) - Y_{min}(i)}{Y_{max}(i) - Y_{min}(i)}\right) - 1 \tag{13}$$

where i represents the case number (from 1 to 950), $X(i)$ and $Y(i)$ represent the original value of the material parameters or response values, the subscripts *min* and *max* present the minimum and maximum values of each parameter or response, respectively, and $X^*(i)$ and $Y^*(i)$ denote the normalized data. This normalization is performed for all of the 18 material parameters (X) and the 3 aspects of reservoir response (Y). At the early stage before any gas is produced, $Y^*(i)$ is set to be 0 as both $Y_{max}(i) = Y_{min}(i) = 0$ at that particular time. The normalization process facilitates the calculation by making the data dimensionless. Additionally, it limits the range of data to vary between $[-1, 1]$, and consequently controls the algorithm search domain, which results in less complexity and higher accuracy of the ANN.

Based on the processed data, 20% of the normalized data is selected as the testing data and the remaining 80% is selected as the training data. This data division (i.e., 20/80 percent) is proposed by most of the studies available in the literature (Mia and Dhar, 2016; Ghorbani et al., 2020; Ranasinghe et al., 2017; Premalatha and Arasu, 2016; Panja et al., 2018) to ensure that there are enough testing samples which have not been used during the training process of ANN but used to test its accuracy. However, a higher percentage for testing can also be used if the amount of raw data is large enough. As a result, 760 simulation cases (80% of the 950 simulation cases) are allocated for the training process, and the remaining 190 simulations (20% of the 950 simulation cases) are stored for network testing.

After creating the training dataset and the testing dataset, the basic structure of the neural network is established. In this study, a multilayer perceptron (MLP) is used to implement the ANN. The proposed network structure, as shown in Fig. 6, consists of the dataset, two hidden layers with 10 and 5 neurons, respectively, and the predictions of the reservoir responses. The prediction consists of 3 classes, each with 30 neurons, which represent the simulation results of gas production, water production, and the borehole displacement at the 30 time intervals (0.2-day intervals for 6 days). The hyperbolic tangent sigmoid transfer function (tansig function) was used as the activation functions in the hidden layers. The ANN was first trained using one

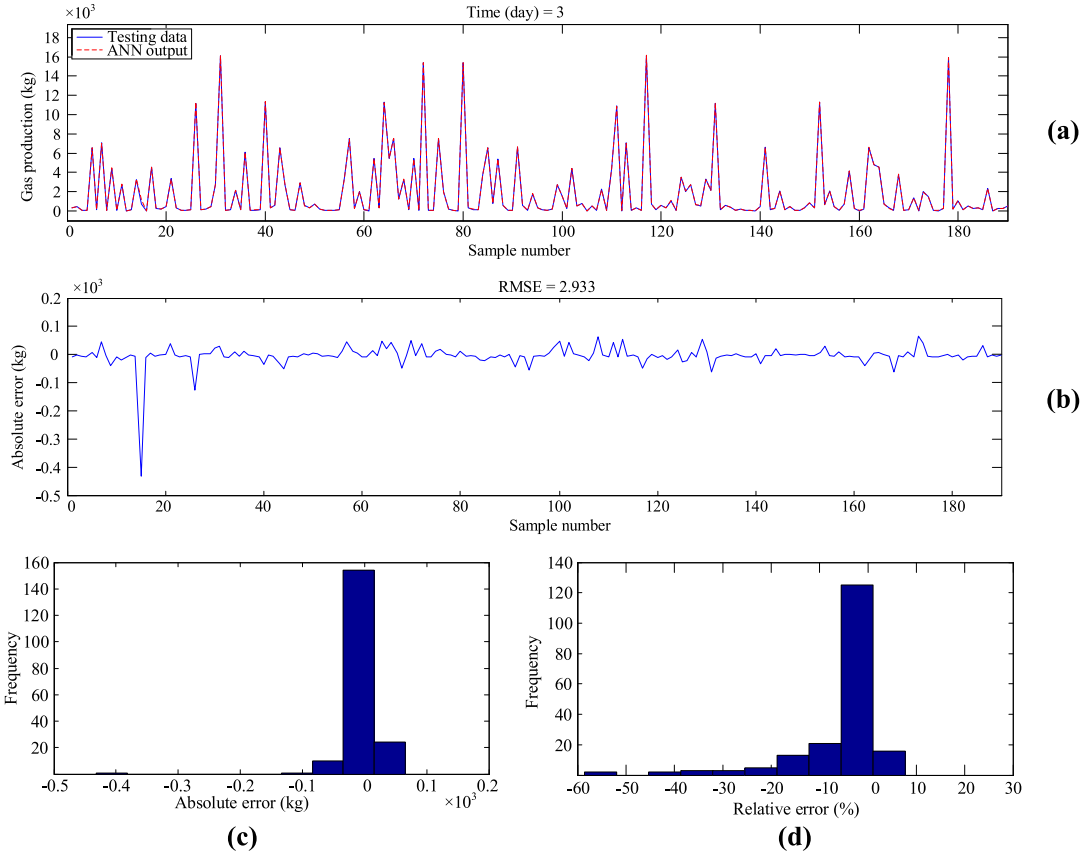

Fig. 8. The analysis output for testing data, reporting (a) primary testing data versus ANN results for t = 3 days, (b) the absolute error, (c) the absolute error histogram, and (d) the relative error histogram.

hidden layer, but it could not achieve satisfactory accuracy even with a large number of neurons in one layer. Therefore, two hidden layers were implemented in this study to accomplish accurate predictions. By adopting a trial-and-error method to adjust the number of neurons in each hidden layer, the MLP model with ten neurons in the first hidden layer and five neurons in the second hidden layer led to a good performance. Thus, the ANN for THM responses was finalized with two hidden layers without adding any further layer.

The initial MLP model was then generated using the training dataset with the proposed layer structure. The training data was introduced into the ANN to train the network by determining the biases and weights through minimization of the root mean squared error (RMSE). Once the minimum RMSE was obtained, the network training process is complete and the ANN can be used to make predictions and its accuracy can be evaluated using the testing data set.

The performance of the neural network was evaluated by comparing the results obtained from the neural network, Y_{ANN}, with the actual primary values, resulted from *FLAC* simulation, Y_{actual}. The comparisons between the predictions from the ANN network and the training data over all the 760 cases for gas production at the third day are presented in Fig. 7(a). The two lines are almost identical and thus Y_{ANN} is only visible in the figure. Similarly, the comparisons between Y_{ANN} and the Y_{actual} for the testing data (= 190 cases) are plotted in Fig. 8(a). The absolute difference between these two, termed herein as absolute error, is calculated as follows: $\delta Y = Y_{actual} - Y_{ANN}$, and plotted in Figs. 7(b) and 8(b), respectively. The relative error is calculated as follows: $\delta e = \frac{Y_{actual} - Y_{ANN}}{Y_{actual}}$. The histograms of the absolute and relative errors are also plotted in Figs. 7(c) & (d) and 8(c) & (d), respectively.

To assess the overall accuracy of the first-block ANN, the whole set of *FLAC* simulation results was plotted against the prediction results obtained from the first-block ANN (Fig. 9). A reference line with gradient of 1 is included on the plot, and shows the almost perfect match between the ANN predicted results and the *FLAC* simulation results. The RMSE values for the training and testing dataset for all three prediction results are computed and summarised in Table 2. The RMSE values for both the training and the testing sets are very small, which suggest that the proposed first-block ANN can make accurate predictions.

By combining the predicted results of the first-block ANN into a single vector, the predicted time histories can be compiled for the first 6 days. The time history of 3 simulations (Case #300, #600 and #900) out of the 950 simulations were plotted in Fig. 10 and compared with the corresponding *FLAC* THM simulation results. The comparison suggests that the resulting time history matched well between the simulation results and the first-block ANN predictions.

3.2. The ANN for forward prediction

The second-block ANN adopts the prediction results of the first six days from the first block to predict the future reservoir responses. Therefore, a time history prediction is required in the second block and is implemented by an incremental algorithm.

Based on the data imported from the first-block ANN, there is only one data point available at each 0.2 day, i.e., 30 data points for the whole six days. This amount of data may not be large enough to allow the second-block ANN to learn the trend of the target time history

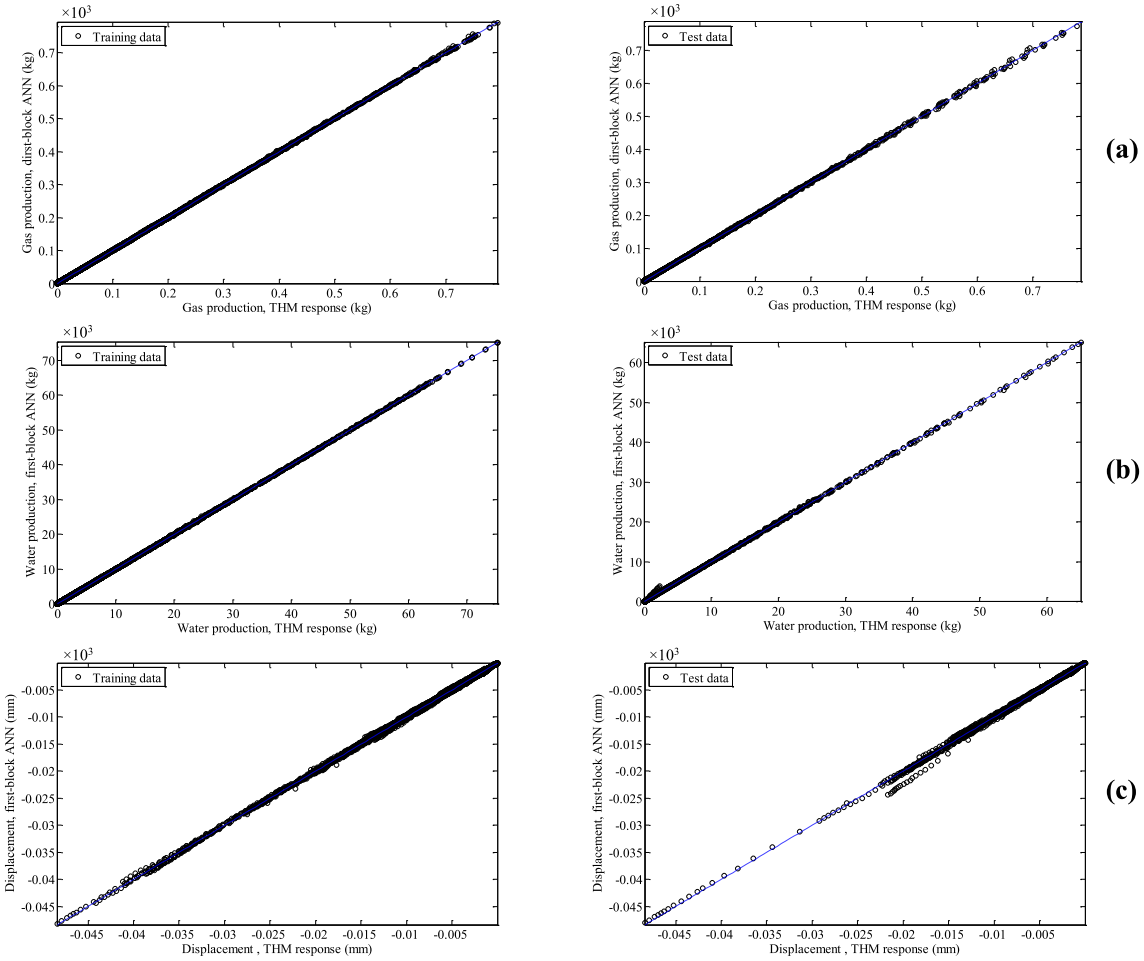

Fig. 9. Simulation results against the ANN predictions for (a) gas production, (b) water production, and (c) borehole displacement.

Table 2
RMSE values of the three prediction results.

Predictions	RMSE for training data	RMSE for test data
Gas production (kg)	2.324	2.933
Water production (kg)	2.569	4.123
Borehole displacement (mm)	0.124	0.145

effectively. To resolve this issue, an up-sampling process is implemented to extract more data from the time history and feed it into the learning process of the second-block ANN. For this purpose, the interval between each two time step is divided into 10 smaller intervals, and the corresponding data points are estimated via linear interpolation. Therefore, the new time step is set to be $dt = 0.02$ days, and 300 data points are stored for each input time history. A smaller time step enriches the training and testing dataset for the second-block ANN, which subsequently helps obtain better convergence and estimation results with smaller computational errors. The results of the up-sampling process for water production data (Case #300) is shown in Fig. 11.

Denoting the resulting time history as a sequence of data, i.e., $\{Y_1, Y_2, ..., Y_n\}$, it can be assumed that each component of the sequence depends on a set of previous responses. For example, taking the response at each time step as a function of those in the five preceding steps, a new equation can be established as follows: $Y_n = f(Y_{n-1}, Y_{n-2}, Y_{n-3}, Y_{n-4}, Y_{n-5})$. Extending this assumption over the entire time series:

$$\begin{aligned} Y_{n-1} &= f(Y_{n-2}, Y_{n-3}, Y_{n-4}, Y_{n-5}, Y_{n-6}) \\ Y_{n-2} &= f(Y_{n-3}, Y_{n-4}, Y_{n-5}, Y_{n-6}, Y_{n-7}) \\ &\vdots \\ Y_6 &= f(Y_5, Y_4, Y_3, Y_2, Y_1) \end{aligned} \tag{14}$$

This set of equations can be rewritten in matrix form as follows:

$$\begin{bmatrix} Y_n \\ Y_{n-1} \\ \vdots \\ Y_1 \end{bmatrix} = f\left(\begin{bmatrix} Y_{n-1} & Y_{n-2} & Y_{n-3} & Y_{n-4} & Y_{n-5} \\ Y_{n-2} & Y_{n-3} & Y_{n-4} & Y_{n-5} & Y_{n-6} \\ & & \vdots & & \\ Y_5 & Y_4 & Y_3 & Y_2 & Y_1 \end{bmatrix} \right). \tag{15}$$

Next, by assuming the right-side matrix as input data and the left-side vector as target data, the second-block ANN is trained with a hidden layer consists of 5 neurons to estimate the function $f(.)$. Then, this neural network can approach the target parameter value one step ahead as follows: $Y_{n+1} = f(Y_n, Y_{n-1}, Y_{n-2}, Y_{n-3}, Y_{n-4})$ (Fig. 6).

For instance, the prediction of the first 6 days obtained from the first block is used in the second block to estimate the function $f(.)$ and consequently predict the responses at step $t = 6.02$ day. 240 time step data points were used as the training data (80% of the 300 data points for the 6-day simulation) and 60 time step data points were used as the testing data (20% of the 300 data points for the 6-day simulation). Fig. 12 shows the training and testing data versus the output of the second-block ANN for the case number 300. A reference line with

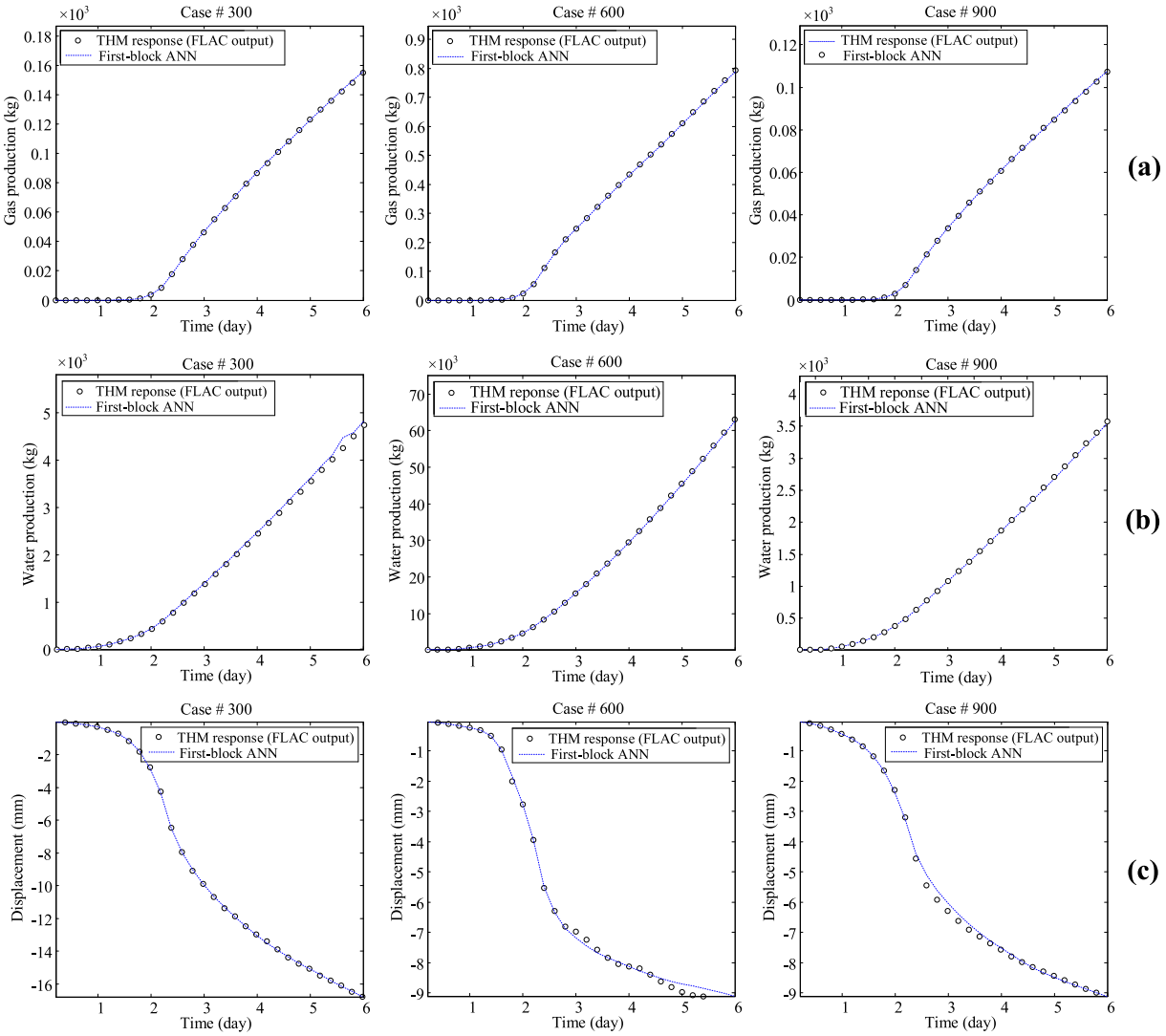

Fig. 10. Results of the ANN in estimating the time history of (a) gas production, (b) water production, (c) borehole displacement.

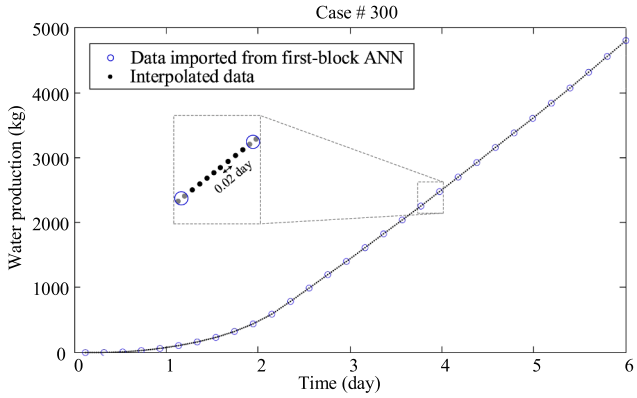

Fig. 11. Dividing each time step into ten 0.02 day intervals.

gradient 1 is drawn on the plot to show the almost perfect positive correlation for both the training data and the testing data. When the accuracy of the second block in estimating the results is ensured, the obtained ANN is used to predict the output at a future time step: $t = 6.02$ day. The predicted result at $t = 6.02$ day is then fed into the second block, to create a new ANN for predicting the next time step at 6.04 day. Therefore, the future data points after six days can be predicted by the second-block ANN through gradually increasing the time increment.

To check the accuracy of the second-block ANN prediction, 8-day predictions for 3 specific cases (Case No. 300, 600, and 900) out of the 950 are simulated via *FLAC*. The corresponding first 6 days gas production, water production and borehole displacements were predicted by the first-block ANN. The first-block ANN prediction results are then fed into the second-block ANN, and the time series predictions are performed to obtain the corresponding results on the 7th and 8th days. The results of the corresponding second block ANN are compared with the simulation outputs as shown in Fig. 13. The first-block ANN represented by the blue line gives the first 6-day prediction, and the second-block ANN represented by the red line gives the prediction results for the seventh and eighth days. Overall, the second-block ANN prediction results matches favorably with the *FLAC* simulation results.

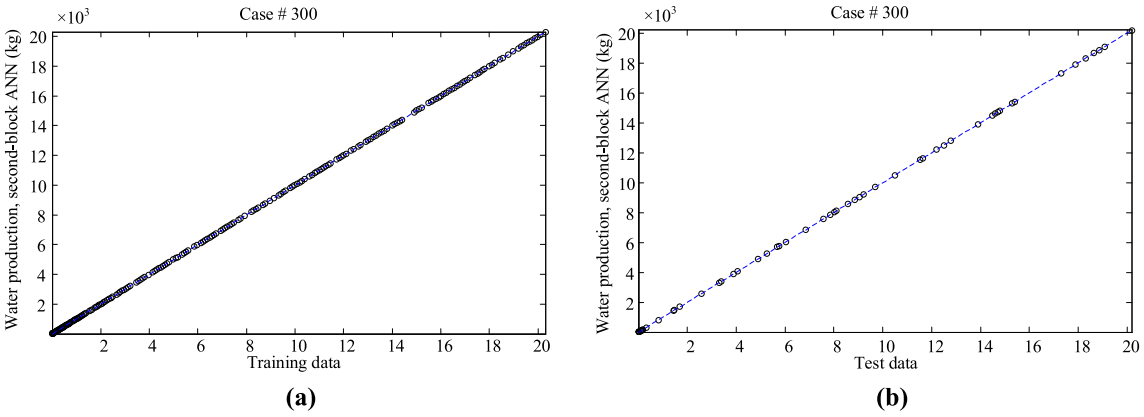

Fig. 12. Water production comparison between the input data and predictions of the second-block ANN for (a) training and (b) testing data.

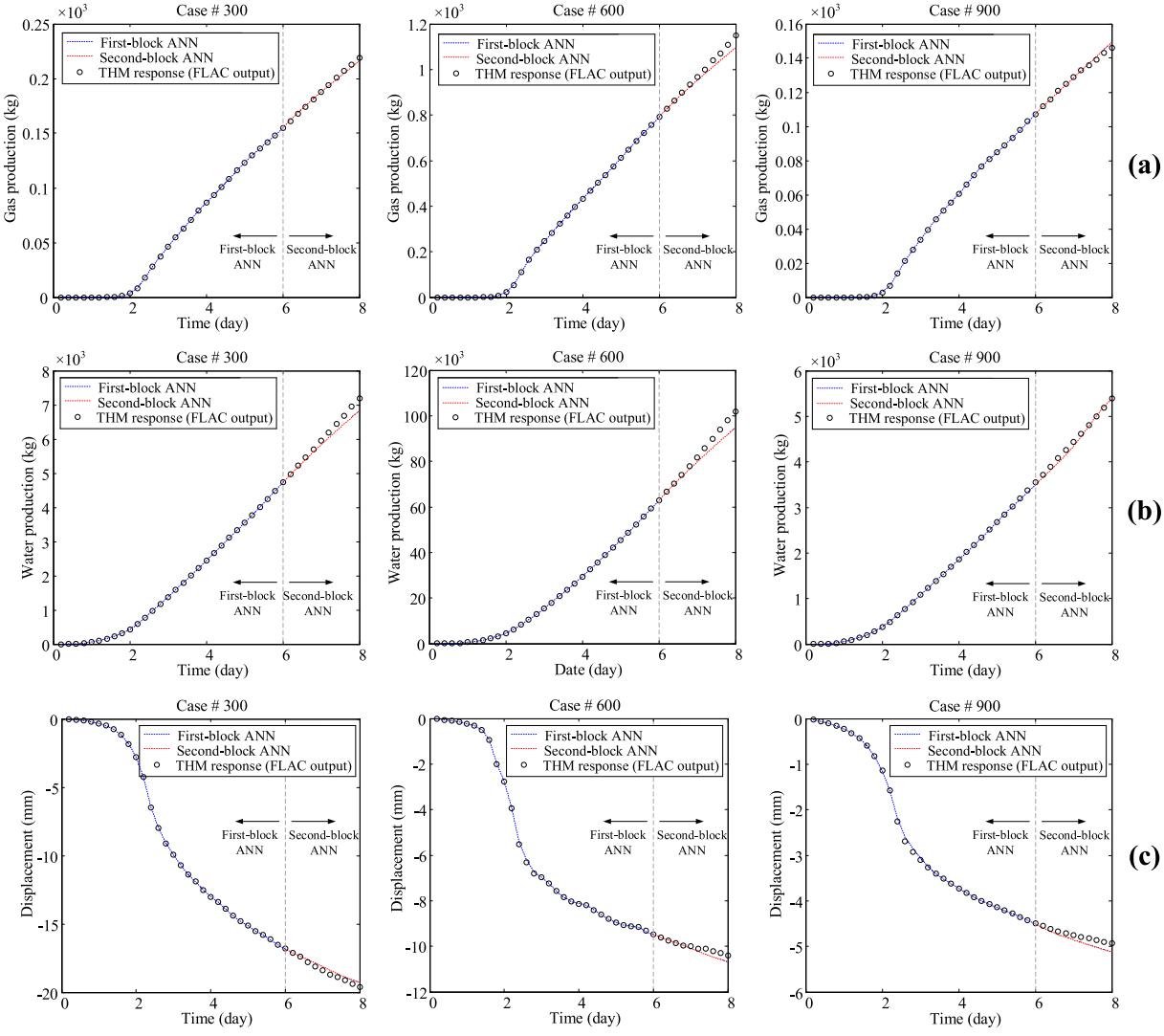

Fig. 13. Results of time-series prediction for (a) gas production, (b) water production, and (c) borehole displacement.

4. Evaluation of execution time

The computational efficiency of the proposed meta-model is demonstrated by comparing its processing time with the *FLAC* THM simulator for three specific reservoir cases (Case 300, 600, and 900). The numerical experiments for 8-day gas production were carried out on a desktop equipped with two GeForce GTX 1080 graphics processing units (GPUs), 64 GB of random access memory (RAM), and one Intel

Table 3
For 6-day gas production prediction, the execution time of the first-block ANN and the *FLAC* THM simulator for Case 300, 600, and 900.

Prediction method	Case 300	Case 600	Case 900
First-block ANN	0.071 s	0.069 s	0.067 s
FLAC THM simulator	1400 s	7000 s	540 s

Core i7-5820 K central processing unit (CPU). For 6-day gas production prediction, the execution time of the first-block ANN and the *FLAC* THM simulator for three specific reservoir cases are shown in Table 3. It is seen that a typical calculating of the *FLAC* THM simulator for 6-day gas production takes on average more than 1000 s while the first-block ANN only takes less than 0.1 s. The variation in the calculation time by the*FLAC* THM simulator is caused by the critical time required for numerical stability associated with monotonic flow (proportional to the element size and inversely related to the permeability and bulk modulus). The computational efficiency of the first-block ANN is ten thousands times faster than the *FLAC* THM simulator. For 6 to 8 day gas production prediction, the second-block ANN takes about 6 s for predicting the reservoir responses at each time increment (0.2 day), whereas the execution time taken by the *FLAC* THM simulator for each 0.2-day interval is on average longer than 10 s.

As for the second-block ANN, it should be mentioned that the training and prediction processes are implemented together in a single loop. That is, after introducing the 6-day data from the first-block ANN into the second-block ANN and performing the interpolation process, a neural network is trained and then used to predict the target value in a step forward. Then, with the new value obtained, the data set is updated, and a new neural network is trained again to predict the target value in the next step. This process is repeated until the target value at the last time point (i.e., day 8) is reached. Since training and prediction are integrated in this implementation, the process takes relatively longer than the first-block ANN (10 min on average). However, this time is still compatible with the time required by the *FLAC* simulator to provide the target values during days 6 to 8 (10 min on average). Even at the current state, the established meta-model is more efficient compared with the *FLAC* THM simulator. This superiority will be even more significant when the simulation considers more complex natures of the hydrate reservoir, since the speed of *FLAC* simulations will depend on size and geometry of model domain, heterogeneity and complexity of constitutive model, while the efficiency of ANN is much less affected by these aspects.

5. Discussions and conclusions

This paper proposes a meta-model consisting of two-block neural network models for simulation of gas production operations in methane hydrate-bearing reservoir. The first-block learns the relationship between the material properties and the reservoir responses, while the second-block explores the evolution of reservoir responses with time. The main advantage of this meta-model lies on its computational efficiency, which is thousands of times faster than the more sophisticated *FLAC* THM simulator. The precise time taken by the *FLAC* THM simulator is case-dependent, whereas the meta-model is much less dependent on modeling features.

Notwithstanding the vast potential of the meta-models, it should be noted that ANN only learns what it is being taught. Its ability to predict the reservoir responses hinges on the fixed time frame modelled by the *FLAC* THM simulator which creates the training dataset. Reservoir responses are dynamically changing throughout different gas production periods, and various mechanisms may evolve with time. Therefore, only a limited future period can be reasonably predicted by the established meta-model. For example, it is not realistic to use 6-day production data to extrapolate to weeks or months of future predictions.

It is important to reiterate that the 18 hydro-mechanical model parameter values, and the associated ranges adopted in this study, may be considered as 'site specific' parameters. Therefore, the established meta-model is applicable only to these site conditions and is not meant to be universal. Moreover, there are 40 additional thermo-hydro-chemo-mechanical model parameters and state variables that are also essential for accurately predicting the hydrate reservoir responses. A future research is planned to develop a comprehensive meta-model for various site conditions by incorporating all the 58 model parameters and state variables presented in Table 1 and Table A.1 with universally applicable ranges. This general model would also enable evaluation of the sensitivity of all input variables and the extent to which each of them affects the hydrate reservoir response.

Establishment of the meta-model is particularly important for the simulation of gas production from hydrate-bearing sediments, which involves significant uncertainties arising from in situ material heterogeneity and the interactions among multiple aspects of the coupled responses. This efficient tool allows real-time prediction to be made and adjusted according to the concurrently observed reservoir response as the process evolves with time at the production site. In a practical situation, the meta-model can be developed at the planning stage, prior to the site operations, using a series of fully-coupled simulations, which physically captures the material response and system uncertainty. Once the meta-model is established, it can be updated and adapted by back-analyses of concurrently measuring data as gas production commences, and the updated model with refined parameters then facilities improved and reliable predictions of the future system response. This concept will be explored in a future study.

Declaration of Competing Interest

None.

Acknowledgement

The work described in this paper is supported by the Natural Science Foundation Committee Program of China (No. 4190724), the fellowship of China Postdoctoral Science Foundation (No. 2020T130471), the Key innovation team program of innovation talents promotion plan by MOST of China (No. 2016RA4059), and the NSFC/RGC Joint Research Scheme sponsored by the National Natural Science Foundation of China and the Research Grants Council of Hong Kong (Project No. N_PolyU518/16).

Appendix A

Table 4

Table 4
Additional thermo-hydro-chemo-mechanical parameters and state variables required for the *FLAC* THM simulation.

Name	symbol	Value
A_{hs}	Methane hydrate surface area	0.375×10^6 1/m
c_g^T	Specific heat capacity of methane gas	$1240 + 3.13T$ J/(kg·K)
c_h^T	Specific heat capacity of hydrate	2010 J/(kg·K)
c_s^T	Specific heat capacity of sand	800 J/(kg·K)
c_w^T	Specific heat capacity of water	$4020 + 0.58T$ J/(kg·K)
K_d	Hydrate dissociation kinetic	$124000\exp\left(-\frac{78151}{RT}\right)$ mol/(m²·Pa·s)
K_g	Bulk modulus of gas	P_g
$\|\|\mathbf{K}_g^T\|\|$	Thermal conductivity of methane gas	0.0335 J/(m·K·s)
$\|\|\mathbf{K}_h^T\|\|$	Thermal conductivity of methane hydrate	0.622 J/(m·K·s)
$\|\|\mathbf{K}_s^T\|\|$	Thermal conductivity of sand	3.92 J/(m·K·s)
$\|\|\mathbf{K}_w^T\|\|$	Thermal conductivity of water	0.5564 J/(m·K·s)
K_w	Bulk modulus of water	2 GPa
M_g	Molecular mass of methane	16.0 g/mol
M_h	Molecular mass of hydrate	$M_g + N_h M_w$
M_w	Molecular mass of water	18.0 g/mol
n_0	Initial porosity	0.35
N_h	Hydration number	6
P_{eq}	Methane hydrate phase equilibrium pressure	$\exp(39.08 - 8520/T)$ kPa
P_{g0}	Initial pore gas pressure	13 MPa
P_{w0}	Initial pore water pressure	13 MPa
R	Ideal gas constant	8.314 J/(K·mol)
S_{g0}	Initial gas saturation	0
S_{h0}	Initial hydrate saturation	0.5
S_{w0}	Initial water saturation	0.5
T_0	Initial temperature	285 K
ΔH	Enthalpy change by methane hydrate phase change	$56599–16.74T$ J/mol
β_g	Thermal expansion coefficient of gas	$1/T$
β_h	Thermal expansion coefficient of hydrate	4.6×10^{-4} K^{-1}
β_s	Thermal expansion coefficient of sand	1.77×10^{-6} K^{-1}
β_w	Thermal expansion coefficient of water	$(13.41T\text{-}3717)\times 10^{-6}$ K^{-1}
ϵ_0^p	Initial plastic strain vector	$\vec{0}$
μ_g	Methane gas viscosity	$(0.033013T + 1.2312)\times 10^{-6}$ Pa·s
μ_w	Water viscosity	$(-0.039154T + 12.430)\times 10^{-3}$ Pa·s
ρ_g	Density of methane gas	$\frac{P_g M_g}{RT}$
ρ_h	Density of methane hydrate	0.9 Mg/m³
ρ_s	Density of sand grains	2.65 Mg/m³
ρ_w	Density of water	1.0 Mg/m³
σ	Total stress	$\sigma' + \delta\frac{P_w S_w + P_g S_g}{S_w + S_g}$
σ'_{h0}	Initial effective horizontal stress	1.5 MPa
σ'_{z0}	Initial effective vertical stress	3.0 MPa

References

Abu Kiefa, M.A., 1998. General regression neural networks for driven piles in cohesionless soils. J. Geotech. Geoenviron. Eng. 124 (12), 1177–1185. https://doi.org/10.1061/(ASCE)1090-0241(1998)124:12(1177).

Adamowski, J., Chan, H.F., 2011. A wavelet neural network conjunction model for groundwater level forecasting. J. Hydrol. 407, 28–40. https://doi.org/10.1016/j.jhydrol.2011.06.013.

Anderson, B., Hancock, S., Wilson, S., Enger, C., Collett, T., Boswell, R., Hunter, R., 2011. Formation pressure testing at the Mount Elbert gas hydrate stratigraphic test well, Alaska north slope: Operational summary, history matching, and interpretations. Mar. Pet. Geol. 28 (2), 478–492. https://doi.org/10.1016/j.marpetgeo.2010.02.012.

Asghari, V., Fai Leung, Y., Hsu, S.-C., 2020. Deep neural network based framework for complex correlations in engineering metrics. Adv. Eng. Informat. 44, 101058. https://doi.org/10.1016/j.aei.2020.101058.

Bal, L., Buyle-Bodin, F., 2013. Artificial neural network for predicting drying shrinkage of concrete. Constr. Build. Mater. 38, 248–254. https://doi.org/10.1016/j.conbuildmat.2012.08.043.

Boswell, R., 2009. Is gas hydrate energy within reach? Science 325 (5943), 957–958. https://doi.org/10.1126/science.1175074.

Cheng, M.Y., Tsai, H.C., Sudjono, E., 2010. Conceptual cost estimates using evolutionary fuzzy hybrid neural network for projects in construction industry. Exp. Syst. Appl. 37, 4224–4231. https://doi.org/10.1016/j.eswa.2009.11.080.

Dallimore, S.R., Wright, J.F., Yamamoto, K., Bellefleur, G., 2012. Proof of concept for gas hydrate production using the depressurization technique, as established by the JOGMEC/NRCan/Aurora Mallik 2007–2008 gas hydrate production research well program, Mackenzie Delta, Northwest Territories, Canada. Bull. Geol. Surv. Canada 601, 1–15. https://doi.org/10.4095/291751.

Ghorbani, B., Arulrajah, A., Narsilio, G., Horpibulsuk, S., 2020. Experimental and ann analysis of temperature effects on the permanent deformation properties of demolition wastes. Transport. Geotech., vol. 24. doi:https://doi.org/10.1016/j.trgeo.2020.100365.

Goh, A.T.C., 1995. Empirical design in geotechnics using neural networks. Géotechnique 45 (4), 709–714. https://doi.org/10.1680/geot.1995.45.4.709.

Goh, A.T.C., 1996. Pile driving records reanalyzed using neural networks. J. Geotech. Eng. 122 (6), 492–495. https://doi.org/10.1061/(ASCE)0733-9410(1996)122:6(492).

Goh, A.T.C., Wong, K.S., Broms, B.B., 1995. Estimation of lateral wall movements in braced excavations using neural networks. Can. Geotech. J. 32 (6), 1059–1064. https://doi.org/10.1139/t95-103.

Gupta, S., Helmig, R., Wohlmuth, B., 2015. Non-isothermal, multi-phase, multi-component flows through deformable methane hydrate reservoirs. Comput. Geosci. 19 (5), 1063–1088. https://doi.org/10.1007/s10596-015-9520-9.

Halton, J.H., 1960. On the efficiency of certain quasi-random sequences of points in evaluating multi-dimensional integrals. Numer. Math. 2 (1), 84–90.

Hancock, S.H., Collett, T.S., Dallimore, S.R., Satoh, T., Inoue, T., Huenges, E., Henninges, J., Weatherill, B., et al., 2005. Overview of thermal-stimulation production-test results for the JAPEX/JNOC/GSC et al. Mallik 5L-38 gas hydrate production research

well. Bull. Geol. Surv. Canada 585, 1–15. https://doi.org/10.4095/220702.
Hashiguchi, K., 1989. Subloading surface model in unconventional plasticity. Int. J. Solids Struct. 25 (8), 917–945. https://doi.org/10.1016/0020-7683(89)90038-3.
Hola, B., Schabowicz, K., 2010. Estimation of earthworks execution time cost by means of artificial neural networks. Autom. Constr. 19, 570–579. https://doi.org/10.1016/j.autcon.2010.02.004.
Itasca Consulting Group, FLAC Manual, 7th Edition.
Jiang, M., Fu, C., Cui, L., Shen, Z., Zhu, F., 2016. DEM simulations of methane hydrate exploitation by thermal recovery and depressurization methods. Comput. Geotech. 80, 410–426. https://doi.org/10.1016/j.compgeo.2016.05.011.
Kewalramani, M.A., Gupta, R., 2006. Concrete compressive strength prediction using ultrasonic pulse velocity through artificial neural networks. Autom. Constr. 15, 374–379. https://doi.org/10.1016/j.autcon.2005.07.003.
Kim, J., Moridis, G., Yang, D., Rutqvist, J., 2012. Numerical studies on two-way coupled fluid flow and geomechanics in hydrate deposits. SPE J. 17 (02), 485–501. https://doi.org/10.2118/141304-PA.
Kimoto, S., Oka, F., Fushita, T., Fujiwaki, M., 2007. A chemo-thermo-mechanically coupled numerical simulation of the subsurface ground deformations due to methane hydrate dissociation. Comput. Geotech. 34 (4), 216–228. https://doi.org/10.1016/j.compgeo.2007.02.006.
Klar, A., Uchida, S., Soga, K., Yamamoto, K., 2013. Explicitly coupled thermal flow mechanical formulation for gas-hydrate sediments. SPE J. 18 (02), 196–206. https://doi.org/10.2118/162859-PA.
Kvenvolden, K.A., 1988. Methane hydrate–a major reservoir of carbon in the shallow geosphere? Chem. Geol. 71 (1–3), 41–51. https://doi.org/10.1016/0009-2541(88)90104-0.
Kvenvolden, K.A., 1998. A primer on the geological occurrence of gas hydrate. Geol. Soc., London, Special Publicat. 137 (1), 9–30. https://doi.org/10.1144/GSL.SP.1998.137.01.02.
Kvenvolden, K.A., Rogers, B.W., 2005. Gaia's breath - Global methane exhalations. Mar. Pet. Geol. 22 (4), 579–590. https://doi.org/10.1016/j.marpetgeo.2004.08.004.
Lee, J., Byun, J., Kim, B., Yoo, D.-G., 2017. Delineation of gas hydrate reservoirs in the ulleung basin using unsupervised multi-attribute clustering without well log data. J. Nat. Gas Sci. Eng. 46, 326–337.
Li, L., Song, G., Ou, J., 2011. DNN based fault tolerant control of nonlinear structural vibration with actuator faults. Adv. Struct. Eng. 14, 871–879. https://doi.org/10.1260/1369-4332.14.5.871.
Lin, N., Zhang, D., Zhang, K., Wang, S., Fu, C., Zhang, J., Zhang, C., 2018. Predicting distribution of hydrocarbon reservoirs with seismic data based on learning of the small-sample convolution neural network. Chin. J. Geophys. 61 (10), 4110–4125.
Liu, X., Flemings, P.B., 2007. Dynamic multiphase flow model of hydrate formation in marine sediments. J. Geophys. Res.: Solid Earth, vol. 112 (B3), b03101. doi:10.1029/2005JB004227.
Makogon, Y.F., Omelchenko, R.Y., 2013. Commercial gas production from Messoyakha deposit in hydrate conditions. J. Nat. Gas Sci. Eng. 11, 1–6. https://doi.org/10.1016/j.jngse.2012.08.002.
Masuda, Y., Naganawa, S., Fujita, K., Sato, K., Hayashi, Y., 1999. Modeling and experimental studies on dissociation of methane gas hydrates in berea sandstone cores. In: Proceedings of the 3rd International Conference on Gas Hydrate, Vol. 1, 1999, pp. 23–31.
McCartney, J.S., Sánchez, M., Tomac, I., 2016. Energy geotechnics: Advances in subsurface energy recovery, storage, exchange, and waste management. Comput. Geotech. 75, 244–256. https://doi.org/10.1016/j.compgeo.2016.01.002.
McKay, M.D., Beckman, R.J., Conover, W.J., 1979. A comparison of three methods for selecting values of input variables in the analysis of output from a computer code. Technometrics 21 (2), 239–245.
Mia, M., Dhar, N.R., 2016. Response surface and neural network based predictive models of cutting temperature in hard turning. J. Adv. Res. 7 (6), 1035–1044. https://doi.org/10.1016/j.jare.2016.05.004.
Momeni, E., Nazir, R., Armaghani, D.J., Maizir, H., 2015. Application of artificial neural network for predicting shaft and tip resistances of concrete piles. Earth Sci. Res. J. 19, 85–93. https://doi.org/10.15446/esrj.v19n1.38712.
Moridis, G.J., Collett, T.S., Pooladi-Darvish, M., Hancock, S., Santamarina, J.C., Boswell, R., Kneafsey, T., Rutqvist, J., Kowalsky, M.B., Reagan, M.T., Sloan, E.D., Sum, A.K., Koh, C.A., 2011. Challenges, uncertainties, and issues facing gas production from gas-hydrate deposits. SPE Reservoir Eval. Eng. 14 (1), 76–112. https://doi.org/10.2118/131792-PA.
Morris, M.D., 1991. Factorial sampling plans for preliminary computational experiments. Technometrics 33 (2), 161–174. https://doi.org/10.2307/1269043.
Ni, S.H., Lu, P.C., Juang, C.H., 1996. A fuzzy neural network approach to evaluation of slope failure potential. Comput.-Aided Civil Infrastruct. Eng. 11 (1), 59–66. https://doi.org/10.1111/j.1467-8667.1996.tb00309.x.
Panja, P., Velasco, R., Pathak, M., Deo, M., 2018. Application of artificial intelligence to forecast hydrocarbon production from shales. Petroleum 4 (1), 75–89. https://doi.org/10.1016/j.petlm.2017.11.003.
Pooya Nejad, F., Jaksa, M.B., 2017. Load-settlement behavior modeling of single piles using artificial neural networks and cpt data. Comput. Geotech. 89, 9–21. https://doi.org/10.1016/j.compgeo.2017.04.003.
Premalatha, N., Arasu, A.V., 2016. Prediction of solar radiation for solar systems by using ann models with different back propagation algorithms. J. Appl. Res. Technol. 14 (3), 206–214. https://doi.org/10.1016/j.jart.2016.05.001.
Ranasinghe, R., Jaksa, M., Kuo, Y., Nejad, F.P., 2017. Application of artificial neural networks for predicting the impact of rolling dynamic compaction using dynamic cone penetrometer test results. J. Rock Mech. Geotech. Eng. 9 (2), 340–349. https://doi.org/10.1016/j.jrmge.2016.11.011.
Rutqvist, J., Moridis, G., Grover, T., Collett, T., 2009. Geomechanical response of permafrost-associated hydrate deposits to depressurization-induced gas production. J. Petrol. Sci. Eng. 67 (1–2), 1–12. https://doi.org/10.1016/j.petrol.2009.02.013.
Saikia, P., Nankani, D., Dutta Baruah, R., 2019. Reservoir facies classification using convolutional neural networks. In: 2019 IEEE Recent Advances in Geoscience and Remote Sensing: Technologies, Standards and Applications, pp. 34–38. https://doi.org/10.1109/TENGARSS48957.2019.8976038.
Sánchez, M., Santamarina, J.C., 2017. THCM coupled model for hydrate-bearing sediments: data analysis and design of new field experiments. Tech. rep., United States Department of Energy (2017).
Sánchez, M., Gai, X., Santamarina, J.C., 2017. A constitutive mechanical model for gas hydrate bearing sediments incorporating inelastic mechanisms. Comput. Geotech. 84, 28–46. https://doi.org/10.1016/j.compgeo.2016.11.012.
Schoderbek, D., Farrell, H., Hester, K., Howard, J., Raterman, K., Silpngarmlert, S., Martin, K., Smith, B., Klein, P., 2013. ConocoPhillips gas hydrate production test final technical report, Tech. rep., United States Department of Energy.
Shahin, M.A., Maier, H.R., Jaksa, M.B., 2002. Predicting settlement of shallow foundations using neural networks. J. Geotech. Geoenviron. Eng. 128, 785–793. https://doi.org/10.1061/(asce)1090-0241(2002)128:9(785).
Shen, J., Chiu, C., Ng, C., Lei, G., Xu, J., 2016. A state-dependent critical state model for methane hydrate-bearing sand. Comput. Geotech. 75, 1–11. https://doi.org/10.1016/j.compgeo.2016.01.013.
Singh, A., Ojha, M., Sain, K., 2019. Predicting lithology using neural networks from downhole data of a gas hydrate reservoir in the Krishna-Godavari basin, eastern Indian offshore. Geophys. J. Int., vol. 220, 3, pp. 1813–1837. arXiv:https://academic.oup.com/gji/article-pdf/220/3/1813/31652823/ggz522.pdf, doi:10.1093/gji/ggz522. URL https://doi.org/10.1093/gji/ggz522.
Sobol', I.M., 1967. Distribution of points in a cube and approximate evaluation of integrals. USSR Comput. Maths. Math. Phys. 7, 86–112.
Sun, X., Nanchary, N., Mohanty, K.K., 2005. 1-D modeling of hydrate depressurization in porous media. Transp. Porous Media 58 (3), 315–338. https://doi.org/10.1007/s11242-004-1410-x.
Tien Bui, D., Tuan, T.A., Klempe, H., Pradhan, B., Revhaug, I., 2016. Spatial prediction models for shallow landslide hazards: a comparative assessment of the efficacy of support vector machines, artificial neural networks, kernel logistic regression, and logistic model tree. Landslides 13 (2), 361–378. https://doi.org/10.1007/s10346-015-0557-6.
Uchida, S., Soga, K., Yamamoto, K., 2012. Critical state soil constitutive model for methane hydrate soil. J. Geophys. Res.: Solid Earth 117 (B3), B03209. https://doi.org/10.1029/2011JB008661.
Uchida, S., Soga, K., Klar, A., Yamamoto, K., 2012. Geomechanical study of the Mallik gas hydrate production field trials. Bull. Geol. Surv. Canada 601, 191–204.
Uchida, S., Xie, X.G., Leung, Y.F., 2016. Role of critical state framework in understanding geomechanical behavior of methane hydrate-bearing sediments. J. Geophys. Res.: Solid Earth 121 (8), 5580–5595. https://doi.org/10.1002/2016JB012967.
Uchida, S., Klar, A., Yamamoto, K., 2016. Sand production model in gas hydrate-bearing sediments. Int. J. Rock Mech. Min. Sci. 86, 303–316. https://doi.org/10.1016/j.ijrmms.2016.04.009.
Uchida, S., Klar, A., Yamamoto, K., 2016. Sand production modeling of the 2013 Nankai offshore gas production test. In: Energy Geotechnics, Taylor & Francis Group, 2016, pp. 451–458.
van Genuchten, M.T., 1980. A closed-form equation for predicting the hydraulic conductivity of unsaturated soils. https://doi.org/10.2136/sssaj1980.03615995004400050002x.
Waite, W.F., Santamarina, J.C., Cortes, D.D., Dugan, B., Espinoza, D.N., Germaine, J., Jang, J., Jung, J.W., Kneafsey, T.J., Shin, H., Soga, K., Winters, W.J., 2009. Physical properties of hydrate-bearing sediments. Rev. Geophys. 47 (4), 1–38. https://doi.org/10.1029/2008RG000279.Table.
Wang, P., Zhu, Y., Lu, Z., Huang, X., Pang, S., Zhang, S., 2014. Gas hydrate stability zone migration occurred in the Qilian Mountain permafrost, Qinghai, Northwest China: Evidences from pyrite morphology and pyrite sulfur isotope. Cold Reg. Sci. Technol. 98, 8–17. https://doi.org/10.1016/j.coldregions.2013.10.006.
Yamamoto, K., Terao, Y., Fujii, T.T., Terumichi, I., Seki, M., Matsuzawa, M., Kanno, T., Corporation, M.N., 2014. Operational overview of the first offshore production test of methane hydrates in the Eastern Nankai Trough. In: Offshore Technology Conference, Offshore Technology Conference, Huston, USA, 2014, pp. 2007–2008. doi:10.4043/25243-MS.
Yilmaz, I., Kaynar, O., 2011. Multiple regression, ANN (RBF, MLP) and ANFIS models for prediction of swell potential of clayey soils. Exp. Syst. Appl. 38, 5958–5966. https://doi.org/10.1016/j.eswa.2010.11.027.
Zhou, M., Soga, K., Yamamoto, K., 2018. Upscaled anisotropic methane hydrate critical state model for turbidite hydrate-bearing sediments at east nankai trough. J. Geophys. Res.: Solid Earth 123 (8), 6277–6298.
Zhou, M., Soga, K., Yamamoto, K., Huang, H., 2018. Geomechanical responses during depressurization of hydrate-bearing sediment formation over a long methane gas production period. Geomech. Energy Environ., doi:https://doi.org/10.1016/j.gete.2018.12.002. URL http://www.sciencedirect.com/science/article/pii/S2352380818300649.